Heron, P.J., et al., 2023, Stranding continental crustal fragments during continent breakup: Mantle suture reactivation in the Nain Province of Eastern Canada: Geology, https://doi.org/10.1130/G50734.1

GSA Supplemental Material

Stranding continental crustal fragments during continental break-up: mantle suture reactivation in the Nain province of Eastern Canada

Philip J. Heron[1], A.L. Peace[2], K.J.W. McCaffrey[3], A. Sharif[1], A. J. Yu[1], and R.N. Pysklywec[4]
[1]University of Toronto Scarborough, Department of Physical and Environmental Sciences, Toronto, ON M1C 1A4, Canada
[2]McMaster University, School of Earth, Environment & Society, Hamilton, ON L8S 4K1, Canada
[3]Durham University, Department of Earth Sciences, Durham DH1 3LE, UK
[4]University of Toronto, Department of Earth Sciences, Toronto, ON M5S 3B1, Canada

Contents:

Supplemental Methods

ASPECT is a geodynamic modelling code that uses the finite-element method to solve the system of equations that describes the motion of a highly viscous fluid. Detail of the code that isn't directly related to the modelling setup specific to this study can be found in the ASPECT user manual (Bangerth et al., 2020) and a recent ASPECT canonical publication (Heister et al., 2017). Computations were done using the ASPECT code version 2.2.0-pre (master, 8df71c585), see Heister et al., 2017, Bangerth et al., 2020, Kronbichler et al., 2012 and Rose et al., 2017.

Experimental setup

The three-dimensional numerical experiments conducted in this manuscript are within a Cartesian box of 400 km (x-axis) by 400 km (y-axis) and 600 km vertically (z-axis). The computational grid on which the visco-plastic Stokes equations are solved is shown in Fig. S2. The computational grid is uniform laterally but varies vertically, with high resolution (1.5 km x 1.5 km x 1.5 km) prescribed in the top 80 km of the model (from the surface to 80 km depth). Below, the resolution is lower (25 km × 25 km × 25 km) from 80 km depth to the bottom of the model (Fig. S2). There are 436k active cells in the model.

The 3D simulations produced 40 million degrees of freedom and needing around 350 GB memory. For most cases, the models used 320 CPUs and took ~22,000 hours of computational time to generate 25 m.y. of deformation on ComputeCanada's Niagara high performance cluster.

Governing equations

In this study, we solve the equations of conservation of momentum, mass and energy after assuming an incompressible medium with infinite Prandtl number (applying the Boussinesq approximation):

$$-\nabla \cdot \left(2\mu\dot{\boldsymbol{\varepsilon}}(\boldsymbol{u})\right) + \nabla \mathrm{p} = \mathrm{p}\mathbf{g} \quad (1)$$
$$\nabla \cdot \boldsymbol{u} = 0 \quad (2)$$
$$\rho C_p\left(\frac{\partial T}{\partial t} + \boldsymbol{u} \cdot \nabla \mathrm{T}\right) - \nabla \cdot k\nabla \mathrm{T} = \rho H. \quad (3)$$

In the equations above, μ is the viscosity, $\dot{\boldsymbol{\varepsilon}}$ is the strain rate tensor, u is the velocity vector, k is the thermal conductivity, ρ is the density, C_p is the thermal heat capacity, H the internal heat production, and T the temperature.

Different material parameters (in this case upper crust, lower crust, mantle lithosphere, asthenosphere, etc.) are represented by *compositional fields* that are advected with the flow (similar to the temperature field). For each field c_i, this formulation introduces an additional advection equation to the system of equations:

$$\frac{\partial c_i}{\partial t} + \boldsymbol{u} \cdot \nabla c_i = 0 \quad (4)$$

Following the Boussinesq approximation, the density varies linearly as a function of the reference density (ρ_0), thermal expansivity (α), reference temperature (T_0), and temperature (T) as an equation of state:

$$\rho = \rho_0\big(1 - \alpha(T - T_0)\big). \qquad (5)$$

The equations above are solved using the finite element method, where the domain is discretized into quadrilateral/hexahedral finite elements and the solution (e.g., velocity, pressure, temperature and compositional fields) is expanded using Lagrange polynomials as interpolating basis functions (as outlined in Glerum et al., 2017). In this study, we employ second order polynomials for velocity, temperature and composition and first order polynomials for pressure (Q2Q1 elements, e.g. Donea and Huerta, 2003). The equations are solved using an iterative Stokes solver (for more details see Kronbichler et al., 2012).

The ASPECT material field *visco-plastic* was used for this study, which is an implementation of a visco-plastic rheology with options for selecting dislocation creep, diffusion creep or a composite viscous flow law. Plasticity limits viscous stresses through a Drucker Prager yield criterion.

The viscosity for dislocation or diffusion creep is defined as:

$$\mu = 0.5A^{-\frac{1}{n}}\, \dot{\varepsilon}_{ii}^{\frac{(1-n)}{n}} exp\left(\frac{E+PV}{nRT}\right) \qquad (6)$$

where A is the prefactor, n is the stress exponent, $\dot{\varepsilon}_{ii}$is the square root of the deviatoric strain rate tensor second invariant, E is activation energy, V is activation volume, P is pressure, R is the gas exponent and T is temperature (e.g., Billen and Hirth, 2007). Here, we select to use the dislocation creep ($v_{(disl)}; n > 1$) equation form.

Viscosity is limited through one of two different 'yielding' mechanisms. Plasticity limits viscous stress through a Drucker Prager yield criterion, where the brittle yield stress in 3D is

$$\sigma_y = \{6C\cos\varphi + 2P\sin\varphi\}/\{\sqrt{3}(3+\sin\varphi)\} \qquad (7)$$

And the ductile yield stress is

$$\sigma_y = A^{-1/n}\, \dot{\varepsilon}_{ii}^{\frac{1}{n}}\, e^{\frac{E+PV}{nRT}} \qquad (8)$$

Above, C is cohesion and φ is the angle of internal friction. If φ is 0, the yield stress is fixed and equal to the cohesion (Von Mises yield criterion). When the viscous stress ($2\mu\varepsilon_{ii}$) exceeds the yield stress, the viscosity is rescaled back to the yield surface $\mu_y = \sigma_y/(2\dot{\varepsilon}_{ii})$, (e.g., Thieulot, 2011). This method of plastic yielding known as the Viscosity Rescaling Method (VRM) (Willett, 1992; Kachanov, 2004) and is implemented by locally rescaling the effective viscosity in such a way that the stress does not exceed the yield stress. In the models here, strain weakening is implemented for the internal friction angle and cohesion – they are linearly reduced by 50% of their value as a function of the finite strain magnitude (from 0.5 to 1.5, Pysklywec et al., 2002) (Table S1).

Table S1. Rheological parameters for *EXP-1*.

Property	Units	UC	LC	ML	A	ML Scar
Density	$kg\ m^{-3}$	2800	2900	3300	3300	3300
Thermal diffusivities	$m^2\ s^{-1}$	1.90476e-6	1.149425e-6	1.010101e-6	1.010101e-6	1.010101e-6
Viscosity prefactor (*A*)	$Pa^{-n}\ s^{-1}$	8.57e-28	7.13e-18	6.52e-16	6.52e-16	6.52e-16
Stress exponent, *n*		4.0	3.0	3.5	3.5	3.5
Activation energies (*Q*)	$kJ\ mol^{-1}$	223	345	530	530	530
Activation volumes	$m^3\ mol^{-1}$	0	0	18e-6	18e-6	18e-6
Thermal expansivities	K^{-1}	2e-5	2e-5	2e-5	2e-5	2e-5
Specific heat	$J\ kg^{-1}\ K^{-1}$	750	750	750	750	750
Heat production	$W\ m^{-3}$	1.0e-6	0.25e-6	0	0	0
Angles of internal friction	^{o}	30 - 15	30 - 15	30 - 15	30 - 15	0
Cohesions	*Pa*	20e6 - 10e6	20e6 - 10e6	20e6 - 10e6	20e6 - 10e6	20e6 - 10e6

Angles of internal friction have strain weakening properties. For models EXP-5, the upper and lower crustal scars have the same properties as the upper crust above, but with a 0^o angle of internal friction. Strain weakening occurs over the range 0.5 to 1.5, in keeping with recent studies (e.g., Pysklywec et al., 2002), with internal friction and cohesion values being decreased by 50% during this range. Abbreviations and citations for composition: UC = upper crust (Gleason & Tullis, 1995); LC = lower crust (Naliboff et al., 2020); ML = mantle lithosphere (Hirth and Kohlstedt, 2004); A = asthenosphere (Hirth and Kohlstedt, 2004). Reference temperature for the densities for all layers is 273K.

Compositional fields (upper crust, lower crust, mantle lithosphere, asthenosphere, and scarring) can each be assigned individual values of thermal diffusivity, heat capacity, density, thermal expansivity and rheological parameters (Table S1). If more than one compositional field is present at a given point (such as for a scar overlain on top of mantle lithosphere), viscosities are averaged with a harmonic scheme (e.g., Glerum et al., 2017).

An initial reference viscosity of 1e+22 *Pa.s* is applied to each compositional field in the models due to the strain rate dependence of viscosity and the lack of an initial guess for the strain rate for the first time-step (Glerum et al., 2017). This initial reference viscosity is starting point to calculate the different viscosity at depth. In testing, we have modified the initial reference viscosity up and down by two orders of magnitude and found no difference in the final outcome of the simulations. During subsequent time-steps, the strain rate of the previous time-step is used as an initial guess for the iterative process. The final effective viscosity is capped by a (user-defined) minimum viscosity (set at 1e+18 *Pa.s*) and maximum viscosity (set at 1e+26 *Pa.s*) to avoid extreme excursions and to ensure stability of the numerical scheme. Although the configuration permits a viscosity range of 8 orders of magnitude, for the majority of models the viscosity profile stays well within this range.

Lithosphere scarring

In the models presented in the main manuscript, the mantle lithosphere scar has an angle of 30 degrees from the horizontal (EXP-1) and extends to a depth of 60 km from the initial starting point 40 km down. This shallow angle is consistent with that indicated from seismic imaging (Cook et al., 2004; Heron et al., 2016b). The mantle lithosphere scar is presumed to be a weak feature, possibly from grain damage processes through ancient deformation. The scar is made weak by prescribing a low value to the internal angle of friction on the structure (0^o) – all other rheological properties are the same as the rest of the layer. In a previous 2D study, the influence of how weak a mantle lithosphere scar needs to be (e.g., changing the value for the angle of internal friction) in the presence of crustal scars was rigorously tested (Heron et al., 2016a; 2016b). Here we build on the findings of the behaviour of lithospheric scars from these previous studies and perform new models in three dimensions. For model EXP-5, the upper and lower crustal scars have the same properties as the upper crust but with a 0^o angle of internal friction.

Time stepping

We use the Courant-Friedrichs-Lewy (CFL) condition to ensure stable convergence. The CFL criterion is set to 0.3 in EXP-1. However, we have tested the model with smaller CFL values (0.2 and 0.1) to ensure the setup is robust (Fig S7).

Rheologies

Table S1 outlines the rheological parameters used for the different compositional layers. The upper crust implements a wet quartzite flow law (Gleason & Tullis, 1995), lower crust applies wet anorthite (Naliboff et al., 2020), and the mantle dry olivine (Hirth and Kohlstedt, 2004). The two upper crust regions for the model North Atlantic Craton and SE Churchill Province are defined as different compositional areas to delineate their geographical position. However, their compositions are the same. Additional model EXP-25 compares a simulation with and without two compositional regions in the upper crust (Fig S18).

All the viscous pre-factors described in Table S1 are scaled to plane strain from uniaxial strain experiments.

Boundary conditions

In the models presented here, we apply a prescribed boundary velocity on the y-axis boundaries (Fig 2 and Fig S3), and tangential velocity boundary conditions on the x-axis boundaries and base walls of the model, as well as a free surface on top. We have modelled the Cartesian 3D box large enough so that deformation driven from the scarring is not influenced by the tangential boundary conditions (as described below).

The prescribed boundary condition on the y-axis (east) wall is a 0.5 cm/yr extension for the lithosphere (120 km) and a return flow of -0.3 cm/yr for the bottom 200 km of the box. In between, the velocity tapers from 0.5 cm/yr to 0 cm/yr from 120 km to 225 km depth, and from 0 cm/yr to -0.3 cm/yr from 200 km to 400 km depth. The reverse is applied to the west wall, with 0.5 cm/yr extension for the lithosphere. After extensive testing, we found this boundary condition to provide stable solutions (Fig S3).

The free surface is formulated by an Arbitrary Lagrangian-Eulerian (ALE) framework for handling motion of the mesh (for more details please refer to Bangerth et al., 2017). All the calculations presented here have 1,281,203 free surface degrees of freedom.

Thermal model setup

An initial temperature field is prescribed (Fig. S1a, b) but is allowed to evolve during the simulation. The initial temperature follows a typical continental geotherm (Chapman, 1986) with no lateral variations. Our initial condition models Cretaceous extension of two connected continental blocks (Fig 1A), which first collided in the Paleoproterozoic (Fig 1Ci-1Cii). The last closure of the oceanic basin to accrete the Churchill Province to the North Atlantic Craton occurred over 1 Ga in the past (Scott, 1998; Fig 1Cii), and therefore there are no thermal perturbations from the tectonic event remaining. Table S2 gives the values for the thermal constraints required to generate the geotherm. As described in Naliboff and Buiter (2015), we use a high conductivity in the asthenosphere to maintain the high adiabat in the layer, and to generate a constant heat flux into the lithosphere (Pysklywec and Beaumont, 2004). The high conductivity however is only applied to the initial geotherm (e.g., Table S2), with the thermal diffusivity properties applied to the layer after the starting temperature starts to evolve (e.g, Table S1).

The temperature equation for calculating the initial geotherm is given as follows:

$$T(z) = T_L + \frac{q}{k} z - \frac{Hz^2}{2k} \qquad (9)$$

where T_L is the temperature at the top of the specific layer, H the heat production, q the heat flow through the surface of the specific layer, k the thermal conductivity and z the depth. The thermal boundary conditions are fixed at 273K at the surface and 1840 K at the base of the model. In addition, we have explored other lithospheric scenarios (e.g., Gouiza and Naliboff, 2021) with a cooler temperature profile at the base of the model, which results in no changes to the tectonics of the system (FIG S13).

Table S2. Thermal parameters for all initial temperature profiles for computing the continental geotherm.

Property	**Units**	**UC**	**LC**	**ML**	**A**
Thickness	*km*	20	20	80	480
Temp top of layer surface	K	273	633	893	1693
Layer surface heat flow	$W\,m^{-2}$	0.055	0.035	0.025	0.012
Thermal conductivity	$W\,(m\,K)^{-1}$	2.5	2.5	2.5	39.25
Heat production	$W\,m^{-3}$	1.0e-6	0.25e-6	0	0

Abbreviations: UC = upper crust; LC = lower crust; ML = mantle lithosphere; A = asthenosphere. Crustal thickness of 40 km is generated from geophysical studies of the area (Funck et al., 2001; Welford and Hall, 2013).

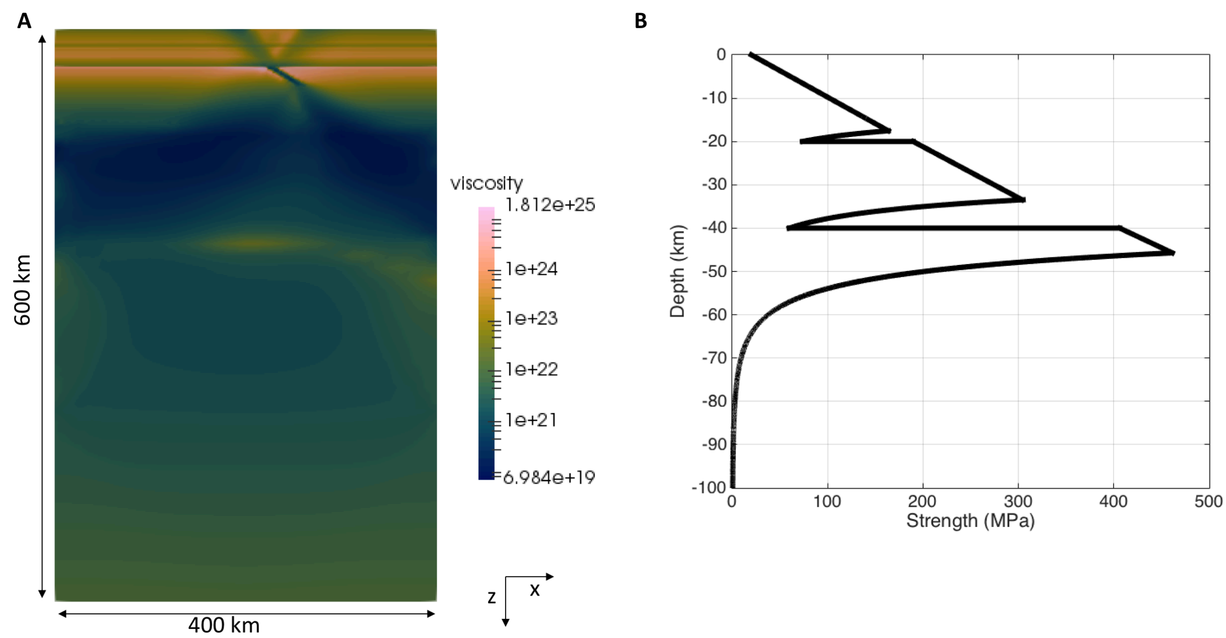

Figure S1. Full viscosity profile (A) in a slice across the middle of the box (f-f' in Fig 3) for *EXP-1*. The lithosphere strength profile for the heterogenous mantle is given in (B), with a strain rate of 1e-14 s^{-1} and the rheological parameters as given in Table S1.

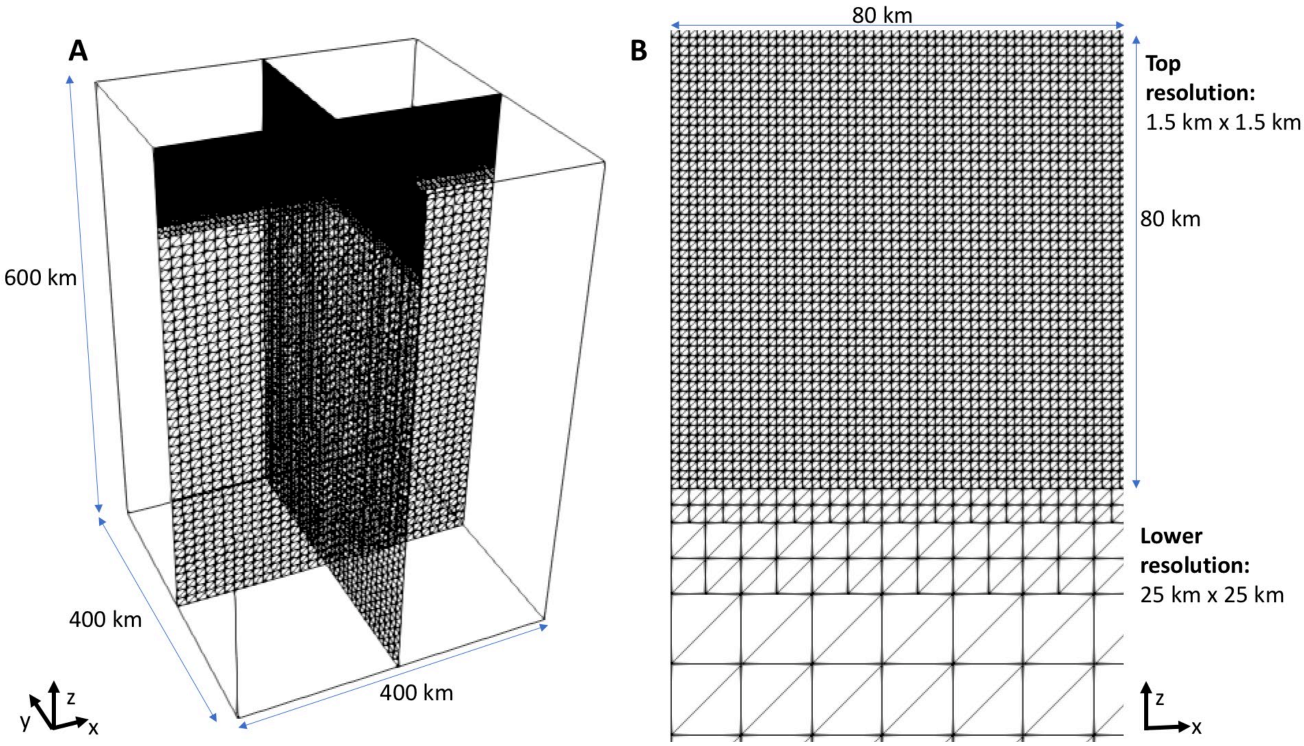

Figure S2. Finite element fixed mesh for all models. There are 436,224 million active cells in the model, with a resolution of ~1.5 km^3 at the surface.

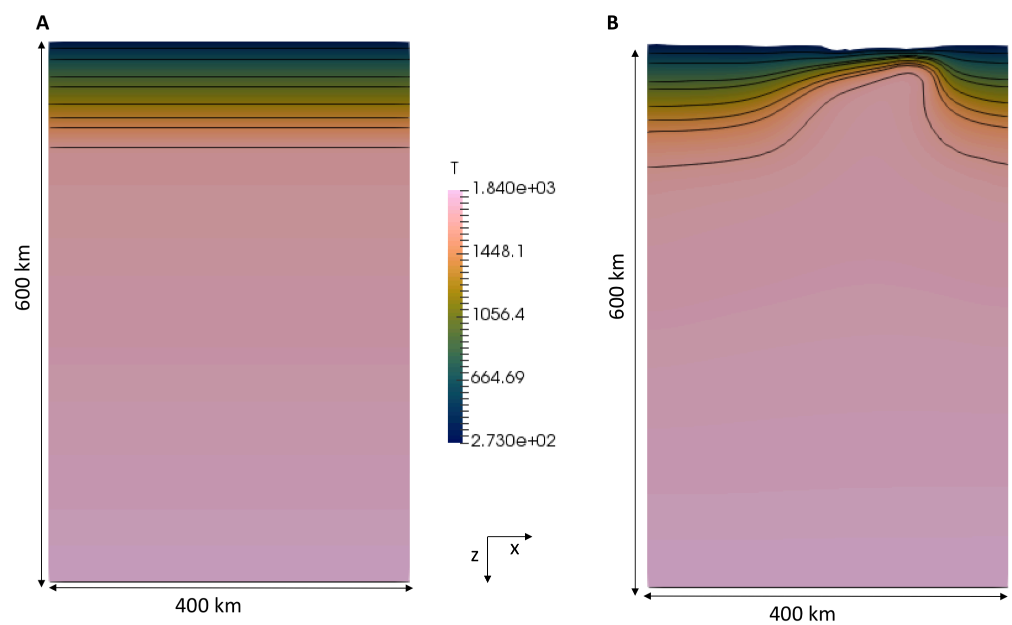

Figure S3. Full temperature profile in a slice across the middle of the box (f-f' in Fig 3) for *EXP-1* for the initial condition (A) and after 20 m.y. (B). The thermal contours for the models are given here as 273 K (surface temperature), 450 K, 633 K (initial base of the upper crust), 893 K (initial base of the lower crust), 1000 K, 1200 K, 1350 K, 1450 K, 1650 K, and 1839.75 K (base of the model).

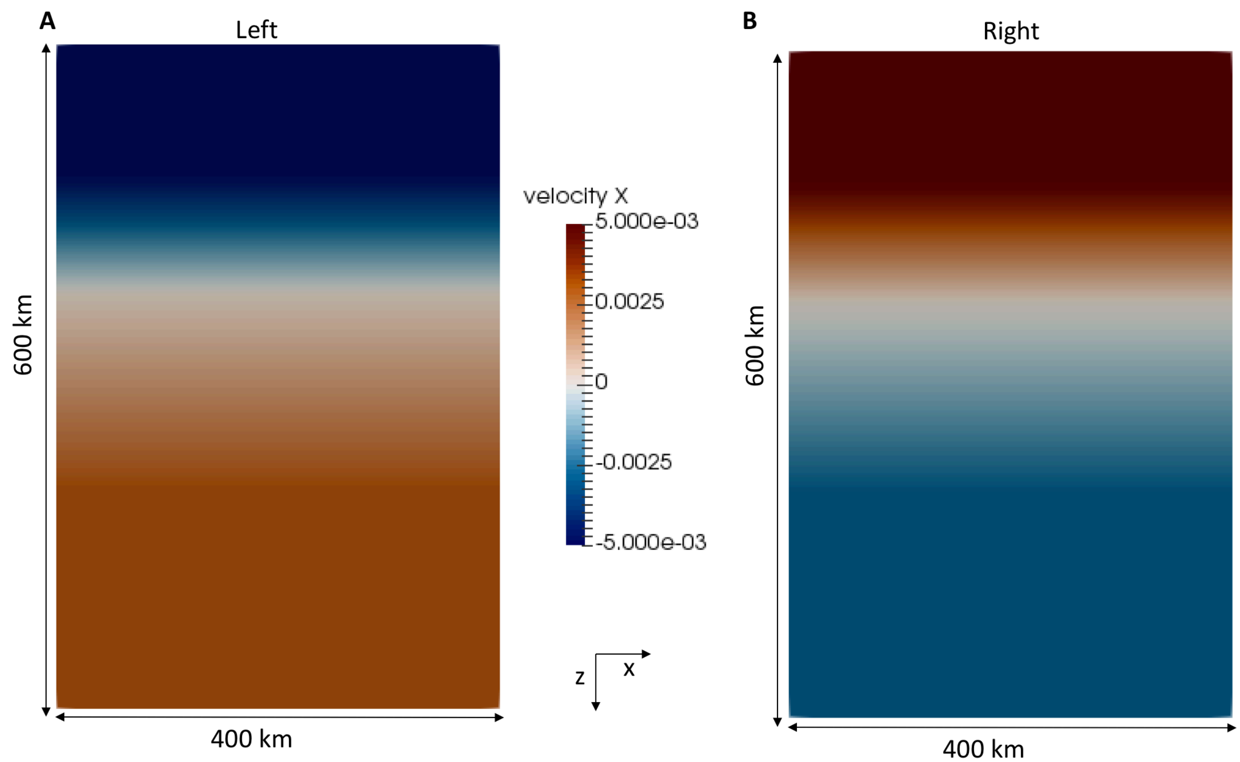

Figure S4. Horizontal velocity condition on the boundaries of the y-axis 'left' (A) and 'right' (B) walls. 0.5 cm/yr of extension is applied to the lithosphere of the 'left' and 'right' walls, which taper down to 0.3 cm/yr of compression for the bottom 200 km of the model.

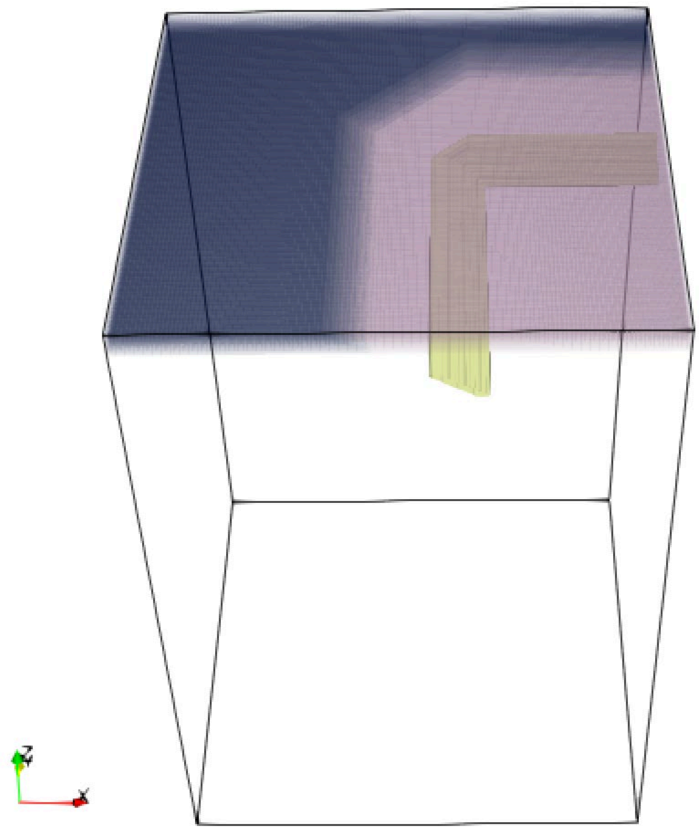

Figure S5: Positioning of mantle lithosphere scar (yellow) with outline of model North Atlantic Craton and Churchill Province upper crust position also shown.

Supplemental Results

In the formulation of this manuscript, we experimented with the sensitivity of the input parameters and how robust the results are (Table S3). In particular, we ran suites of models that looked at:

- Changing the subduction angle of the mantle lithosphere scar;
- Running the reference model EXP-1 with crustal scarring;
- Changing the CFL number and numerical resolution to test for sensitivity;
- Adding in random strain perturbation to the model;
- Modifying the lithospheric temperate and depth;
- Exploring the different strain rate parameters;
- Testing the position of mantle lithosphere scarring;
- Changing the thermal expansivity of the simulations.

Table S3. List of some of the numerical models performed in this study:

Name	Where	Description	Result
EXP-1	Fig 2-3	Main model as described in text	Generation of fragment
EXP-2	Fig 3	Changing subduction angle to 45º	Smaller width of fragment compared to EXP-1
EXP-3	S8	Changing subduction angle to 25º	Larger width of fragment compared to EXP-1
EXP-4	S8	Changing subduction angle to 35º	Smaller width of fragment compared to EXP-3
EXP-5	S9	EXP-1 with UC and LC scars	ML scar dominates and generates same result as EXP-1
EXP-6	S10	EXP-1 with CFL to 0.2	No change to EXP-1 result
EXP-7	S10	EXP-1 with CFL to 0.1	No change to EXP-1 result
EXP-8	S11	EXP-1 with lithosphere resolution increase (to 0.7 km)	No change to EXP-1 result
EXP-9 to EXP-10	S12	EXP-1 with a random perturbation of plastic strain to add a background structural weakness to the models (e.g., Naliboff et al., 2020; Gouiza and Naliboff, 2021).	Focusses strain in the 'northern' section of the model, where there is no weak zone to guide rifting. Same fragment generated as EXP-1
EXP-11	S13	Temperature profile across the model domain reduced as compared to EXP-1 (base of the model 1793K from 1840 K).	No change to EXP-1.
EXP-12	S13	Lithospheric thickness and temperature profile changed to that of Gouiza and Naliboff (2021). Lithospheric thickness increased to 200 km.	No change to EXP-1.
EXP-13	S14	Strength of lower crust rheology	Impacts the timing of fragment

		decreased through changing the viscosity prefactor to values from Rybacki et al. (2006).	generation (later), and reduces the amount of thinning in the upper crust.
EXP-1_2D	S15	2D model of EXP-1 across middle of 3D box (e.g., Fig 3B)	Generation of fragment same as EXP-1
EXP-14	S15	Increasing bottom boundary of ML scar to extend to 80 km depth (from 60 km). 2D model.	Same result as EXP-1_2D
EXP-15	S15	ML scar top boundary at 50km depth rather 40 km, bottom boundary at 50km. 2D model.	Size of fragment remains the same as EXP-1_2D, with additional LC at surface.
EXP-16	S15	ML scar top boundary at 55 km depth, bottom boundary at 75 km. 2D model.	No deformation as scar does not produce any strain localization (as located in viscous part of ML)
EXP-17 to EXP-23	S16	Changing strain weakening parameters, see Table S5 (2D)	Change in shape of rifting, but still generates a continental fragment
EXP-24	S17	Adding in composite rheology: diffusion and dislocation creep. This model also feature random initial strain localization (see EXP-9)	Change in timing and shape of rifting, but still generates a continental fragment
EXP-25	S18	One upper crust composition is applied. 2D model.	No change to result shown in EXP-1_2D.
EXP-26 to EXP-27	S19	Changing thermal expansivity values (2D)	No change to result shown in EXP-1_2D

S denotes the model features in the Supplemental Material. Abbreviations: UC = upper crust; LC = lower crust; ML = mantle lithosphere. 2D models noted in description.

Mechanism for fragment generation

Figure S6 shows the evolution of the strain rate for EXP-1, the reference model, and EXP-2 (which has a steeper mantle lithosphere scar). The process for generating a continental fragment is the same in both models, the only difference is the location of the initial deformation. Initially, the mantle scar creates high strain rate that extends to the crust (Fig S6A). However, as the model begins to deform, the scar becomes less impactful and the it is the location of the shallowest part of the heterogeneity that controls the deformation (Fig S6B). This is highlighted when comparing two models with different dip angles after 5 m.y. (Fig S6B and G). The only difference in the strain rate pattern is the location is different. As EXP-2 has a steeper dip angle, the top of the mantle lithosphere scar is closer to upper crust contact in the horizontal direction. Therefore, a smaller width continental fragment is created. This mechanism is described in more detail in Fig S7.

In Figure S8, we show additional models of the result shown in Figure 3, where decreasing the mantle scar angle increases the width of the continental fragment generated. The results presented here indicate that for a decrease in dip angle by 1 degree we would expect an increase in continental width of approximately 2.5 km. Therefore, extrapolating our models to a shallow angle of 10^{o}, we would expect a continental width of 150 km. Analysis of examples of mantle heterogeneities related to a suture show that angles between 10^{o} and 30^{o} are representative (Cook et al., 2004; Heron et al., 2016b). Given this shallow nature of mantle lithosphere scarring, and the relationship between angle and fragment width, the mechanism proposed here indicates that 100-150 km should be an approximate width for continental terranes (Fig S8).

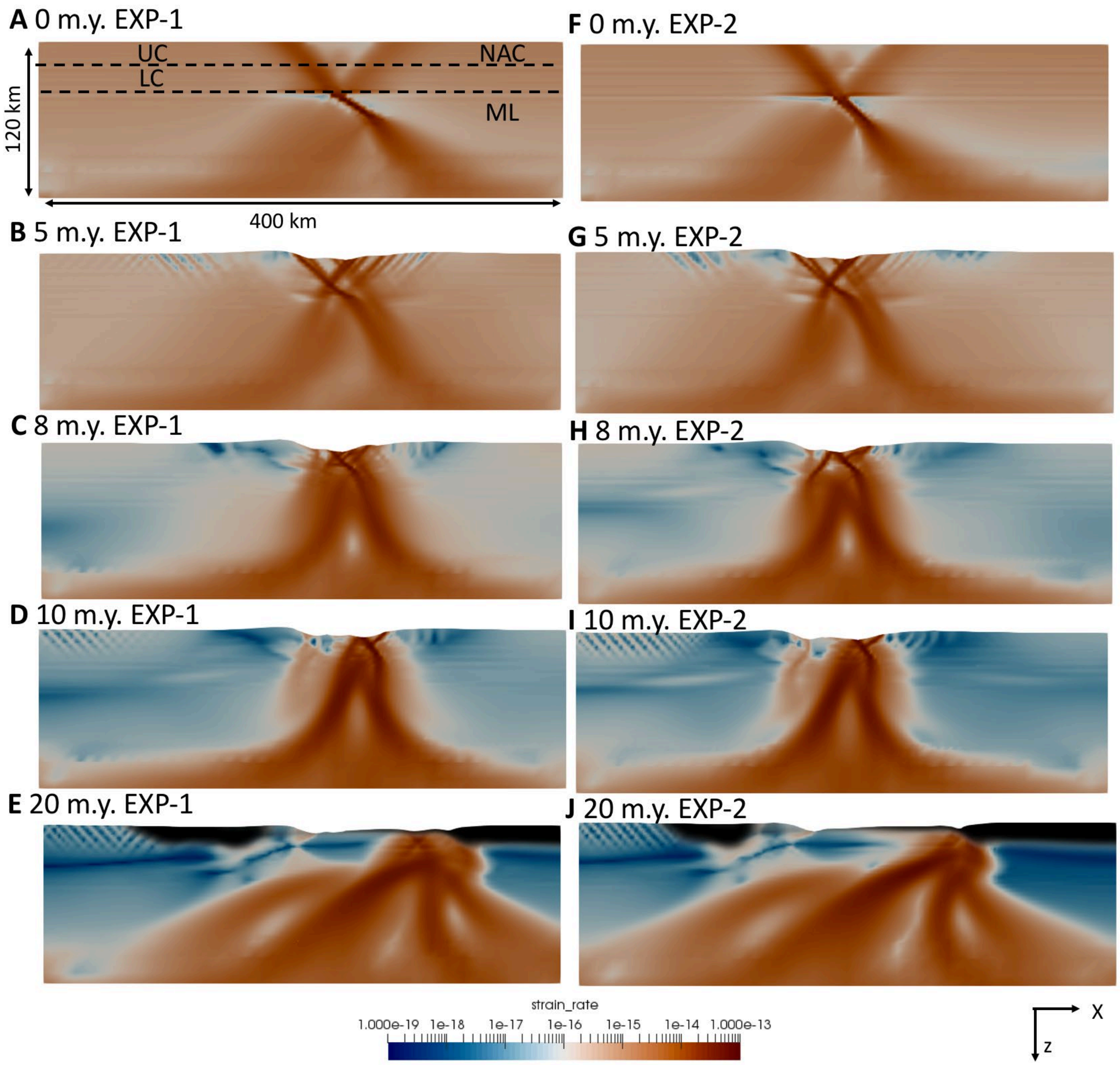

Figure S6: Strain rate evolution for cross-section across the middle of the model domain (e.g., Fig 3B) for scar with 30º dip (EXP-1, A-E) and and 45º (EXP-2, F-J). In E and J, black outlines represent the NAC composition field. The shallower the angle, the larger the fragment generated. Abbreviations: UC = upper crust; LC = lower crust; ML = mantle lithosphere; NP = Nain Province fragment; NAC = North Atlantic Craton.

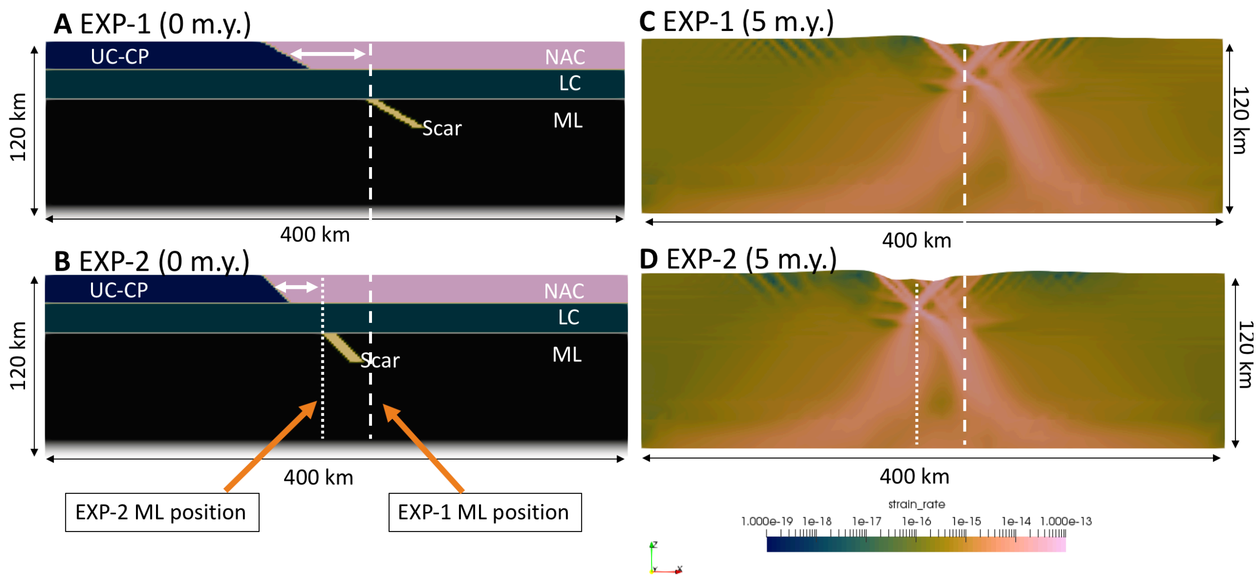

Figure S7: Mechanism for generating different sized continental fragments. A-B shows the initial composition cross-section across the middle of the box. Due to the shallow scar in EXP-1, the top of the mantle scar is a greater distance away from the edge of the NAC than in EXP-2 where the scar is steeper (as shown by white arrows). In C-D, the panels show the strain rate cross-section at 5 m.y., where the deformation for EXP-1 and EXP-2 is similar, but just in different positions. Thick dashed line shows the position of the top of the EXP-1 scar, thin dashed line shows the top position of EXP-2 scar. Abbreviations: UC = upper crust; LC = lower crust; ML = mantle lithosphere; NP = Nain Province fragment; NAC = North Atlantic Craton.

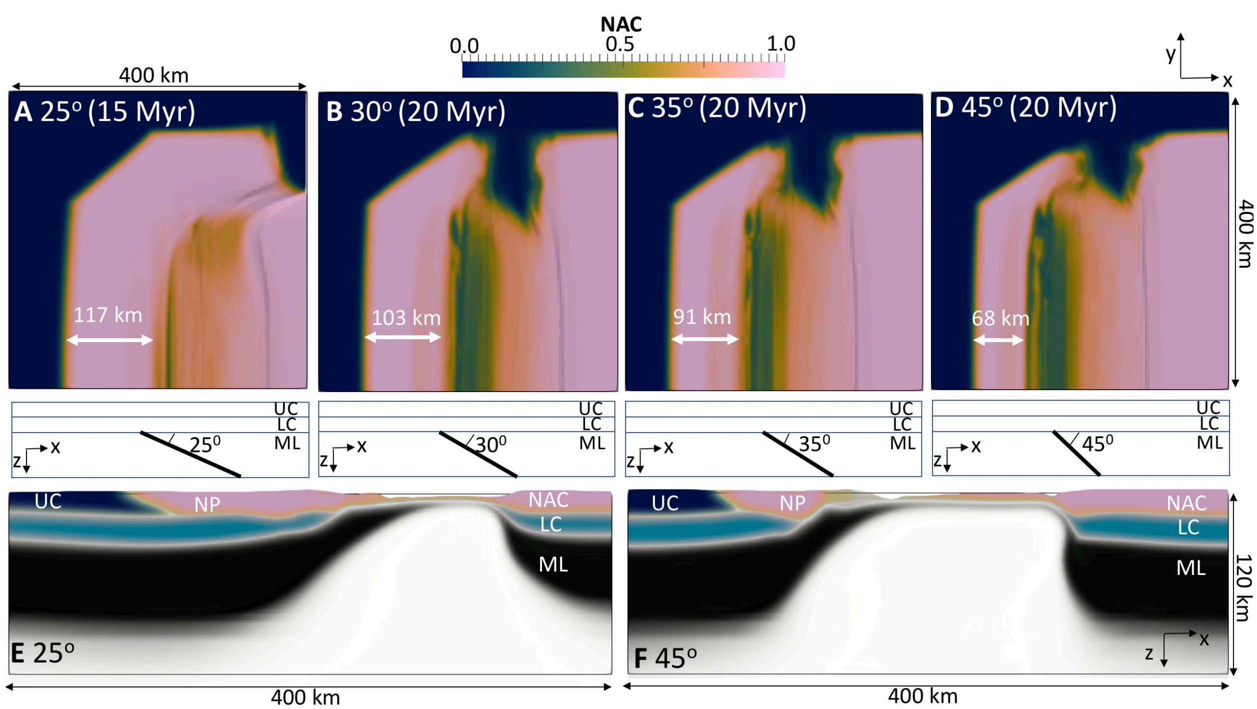

Figure S8: The impact of changing the mantle scar angle (e.g., subduction angle) on the stranding of a continental fragment. A-D shows surface view of the model North Atlantic Craton breakup at 20 m.y. for scar angles (A) 25° (EXP-3); (B) 30° (EXP-1); (C) 35° (EXP-4); and (D) 45° (EXP-2). E-F shows the cross-section view across middle of the simulation for A and D, respectively. The shallower the angle, the larger the fragment generated. Abbreviations: UC = upper crust; LC = lower crust; ML = mantle lithosphere; NP = Nain Province fragment; NAC = North Atlantic Craton.

Crustal scars

In our reference model EXP-1, there is only one location of scarring, placed in the mantle lithosphere. However, it is likely that there would be crustal inheritance as well as deeper deformation. By adding crustal scars to EXP-1, we show a mantle lithosphere scar can still produce a fragment even when crustal inheritance is present (Figure S9). Such results bolster previous findings showing the relative behaviour of inherited deep and shallow deformation features (Heron et al., 2016a, 2016b).

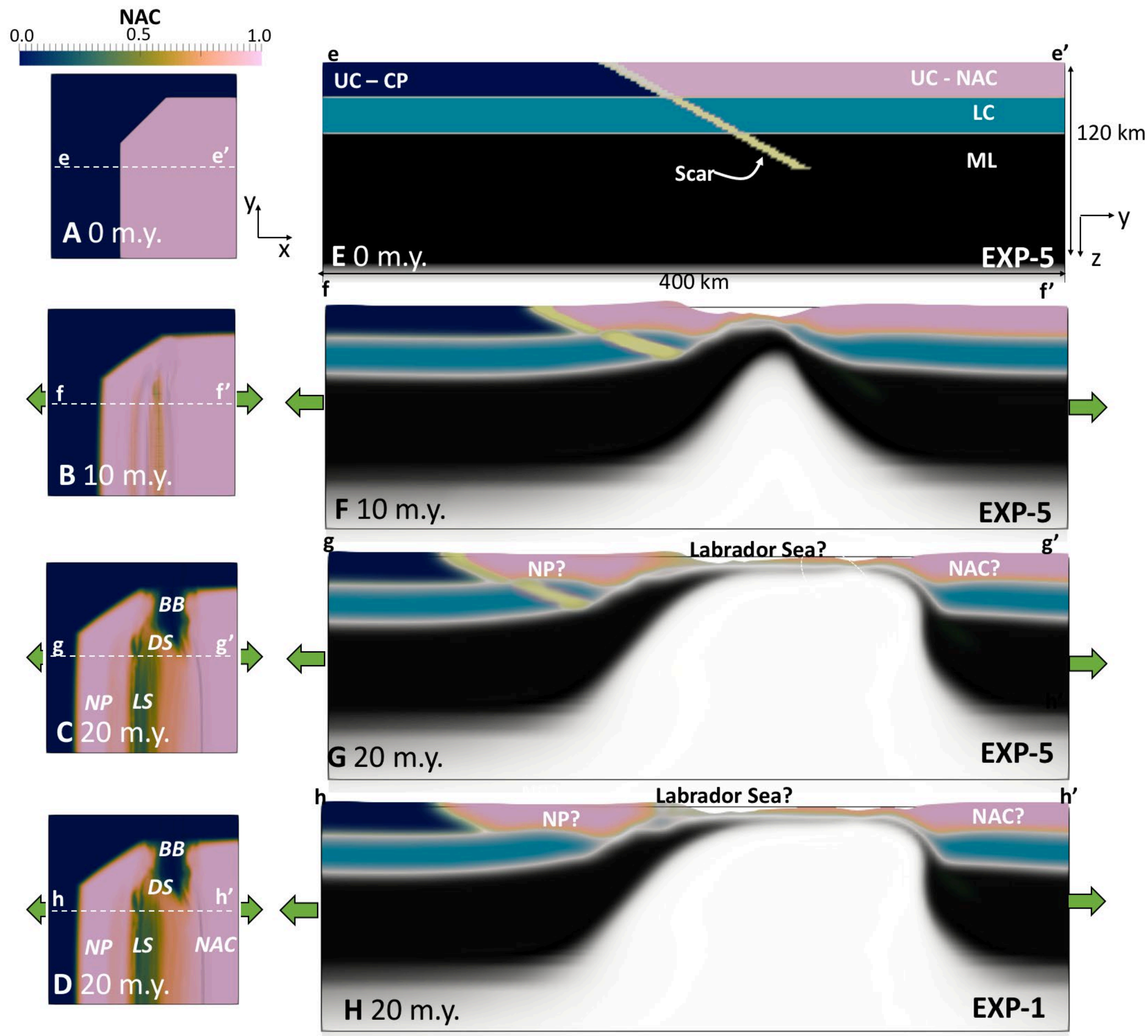

Figure S9: Evolution of rifting from reactivation of mantle lithosphere suture for EXP-5 (30^{o} angle from horizontal) that features upper and lower crustal scars. A-D: Outline of surface deformation for the model North Atlantic Craton (NAC). E-H: Lithosphere cross sections corresponding to lines as shown in A-D. Abbreviations: UC = upper crust; LC = lower crust; ML = mantle lithosphere; AS = asthenosphere; CP = SE Churchill Province; LS = Labrador Sea; NP = Nain Province; DS = Davis Strait; BB = Baffin Bay.

Computational robustness

In order to understand how robust our numerical setup is, we show that decreasing the CFL number does not impact the overall tectonics of the simulation (Figure S10) and that our choice of resolution for EXP-1 was sufficient (Figure S11).

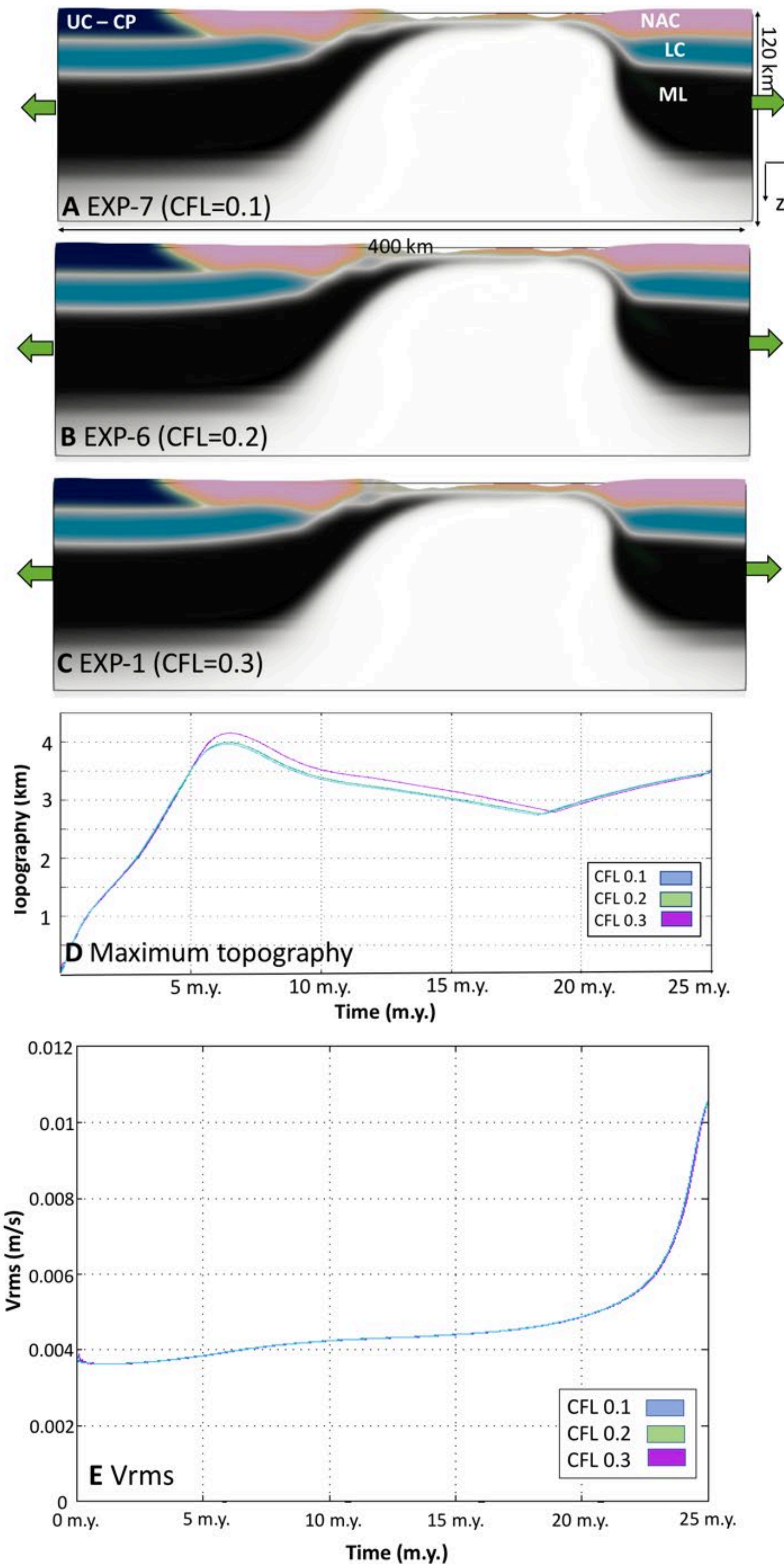

Figure S10: Impact of changing the CFL number on model evolution. A-C shows the lithospheric cross section across the middle of the model domain at 20 m.y. for all simulations. Panel D and E shows the change in maximum topography and root mean squared velocity (Vrms), respectively, as a function of time for the different models. Changing the CFL number has a small impact on topography, but little difference on the overall tectonics of the system. Abbreviations: UC = upper crust; LC = lower crust; ML = mantle lithosphere; AS = asthenosphere; CP = SE Churchill Province; NAC = North Atlantic Province.

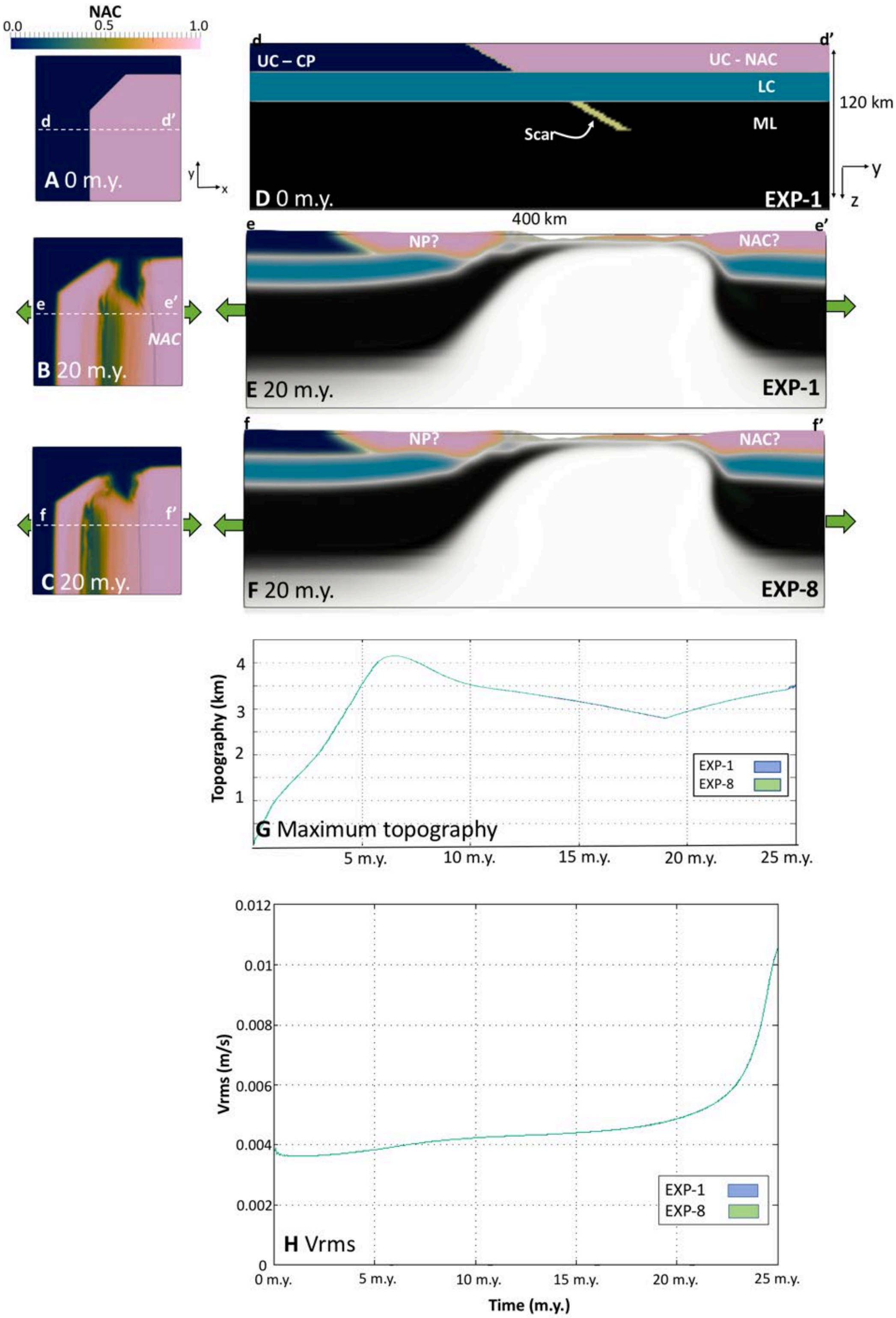

Figure S11: Impact of changing resolution. Evolution of rifting from reactivation of mantle lithosphere suture for EXP-1 (normal resolution) and EXP-8 (increased crust and upper mantle lithosphere resolution). A-C: Outline of surface deformation for the model North Atlantic Craton (NAC). D-F: Lithosphere cross sections corresponding to lines as shown in

A-C. Abbreviations: UC = upper crust; LC = lower crust; ML = mantle lithosphere; AS = asthenosphere; CP = SE Churchill Province. Although the resolution in the top 80 km of the model has increased from 1.5 km^3 in EXP-1 to 0.7 km^3 in EXP-8, there is no noticeable difference in the simulations. Panel G and H shows the time series of the maximum topography and root mean squared velocity (Vrms) of the two models, respectively, showing small differences.

Random plastic strain perturbation

A number of recent studies have introduced a random plastic strain perturbation into the initial profile of the lithosphere (e.g., Naliboff et al., 2020; Gouiza and Naliboff, 2021). In Figure S12, we show the impact of introducing a random plastic strain perturbation which acts as lithospheric inheritance structures (EXP-9). These small-scale random perturbations act to localise strain more easily than models that have a homogeneous initial strain profile (Fig S12). The impact on the models, as compared to the reference EXP-1, is that there is a localisation of strain in the 'northern' section of the surface where there is no mantle lithosphere heterogeneity (Fig S12A-B). This manifests over time as more focused rifting occurring earlier in the simulation (Fig S12E-F) – the 'northern' surface of the model breaks up earlier in the models with a random strain perturbation. However, there is no difference in the mechanism for generating a continental fragment. Another model with random plastic strain perturbation implemented (EXP-10) produced the same results as EXP-9.

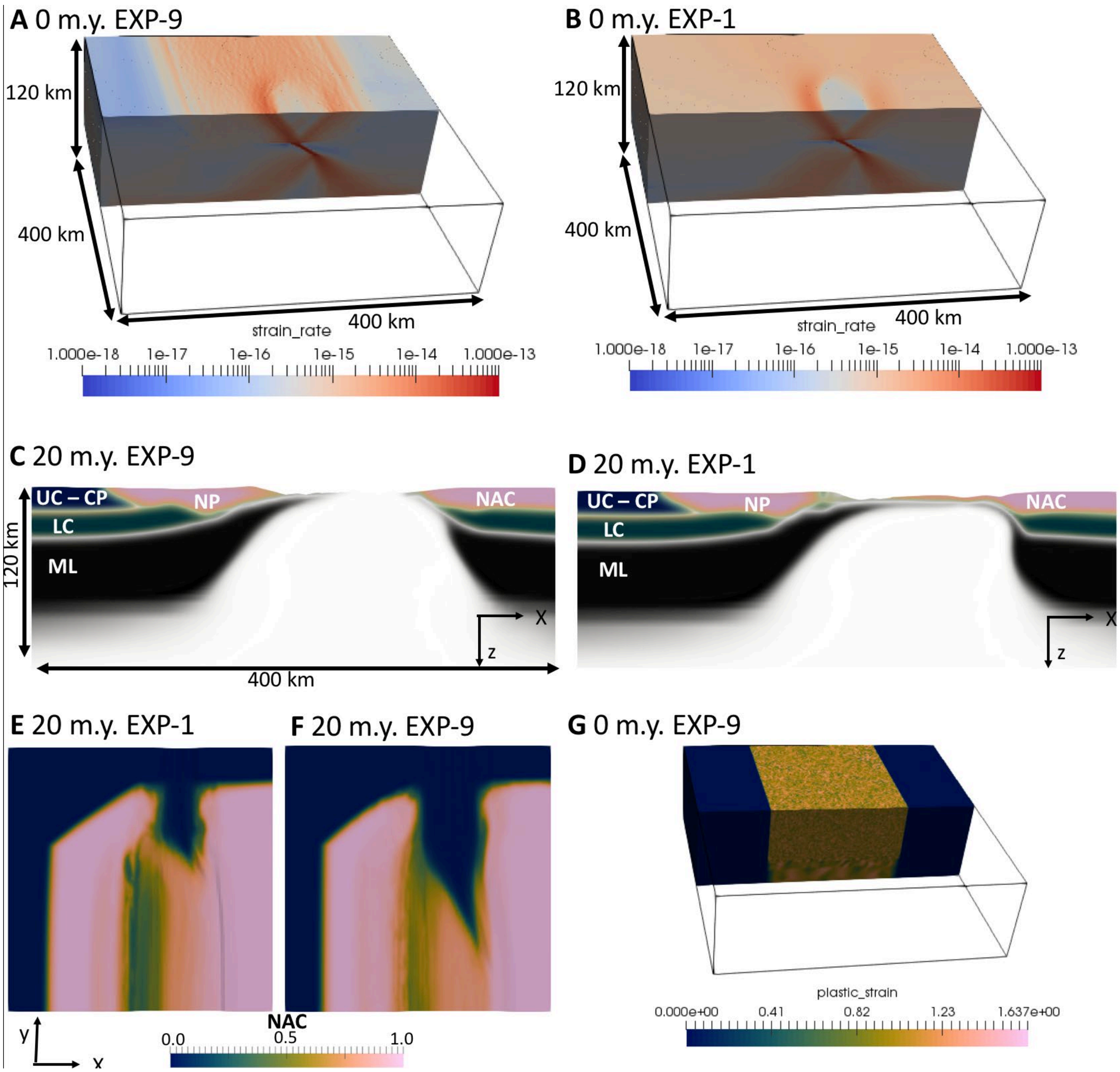

Figure S12: Exploring models that feature a random plastic strain perturbation in the initial condition. A) and B) show strain rate fields for a subsection of EXP-9 and EXP-1 (respectively), where EXP-9 has a random perturbation of plastic strain in the initial setup (panel G). A cross-section of the lithospheric compositional fields shows the generation of continental fragment NP for both EXP-9 (C) and EXP-1 (D). Abbreviations: UC = upper crust; LC = lower crust; ML = mantle lithosphere; AS = asthenosphere; CP = SE Churchill Province; NP = Nain Province. Method for EXP-9 follows Naliboff et al., (2020) and Gouiza and Naliboff (2021).

Lithospheric thickness and structure

In order to test the impact of modifying the lithospheric structure on the mechanism for generating continental fragments, we first changed the mantle temperature (EXP-11) and then the lithospheric thickness (200 km) and temperature (EXP-12). In these models, shown in Figure S13, we implement the temperature profile and thickness similar to that used in Gouiza and Naliboff (2021) as outlined in Table S4. There is no impact on mantle dynamics or for the mechanism of generating a continental fragment.

Table S4. **Thermal parameters for all initial temperature profiles for computing the continental geotherm in additional models EXP-12.**

Property	**Units**	**UC**	**LC**	**ML**	**A**
Thickness	*km*	20	20	160	400
Temp top of layer surface	K	273	633	893	1693
Layer surface heat flow	$W\ m^{-2}$	0.055	0.035	0.015	0.25
Thermal conductivity	$W\ (m\ K)^{-1}$	2.5	2.5	3.0	1000.0
Heat production	$W\ m^{-3}$	1.0e-6	0.25e-6	0	0

Surface temperature set at 273 K and basal temperature at 1793 K. Abbreviations: UC = upper crust; LC = lower crust; ML = mantle lithosphere; A = asthenosphere.

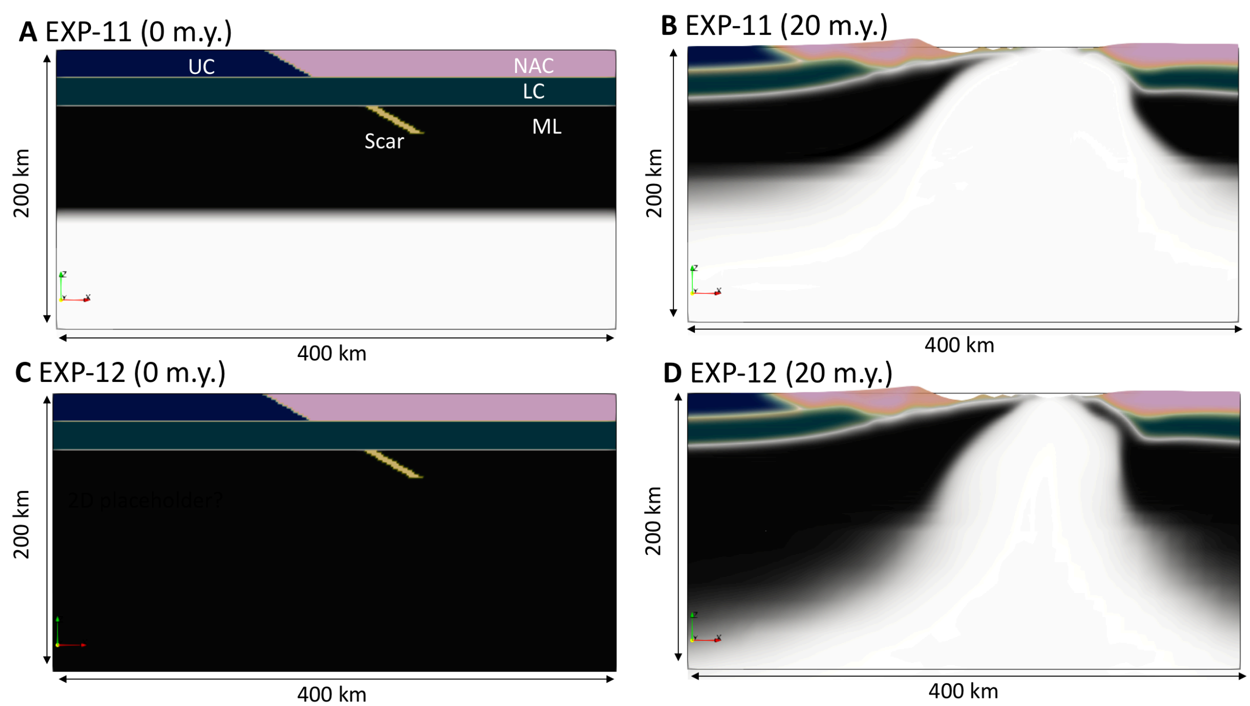

Figure S13: Impact of changing the initial temperature profile to have a cooler base of the model (A-B, EXP-11, Table S4) and then applying a thicker lithosphere (C-D, EXP-12, lithospheric thickness from 120 km to 200 km). Abbreviations: NAC = North Atlantic Craton; UC = upper crust; LC = lower crust; ML = mantle lithosphere.

In Figure S14, we explore the strength of the lower crust. In EXP-1 we implement a lower crust as applied from Naliboff et al. (2020) and in comparison we apply rheological parameters related to Rybacki et al. (2006) in EXP-13 (which takes into consideration the water fugacity of the wet anorthite and reduces the strength of the lower crust). As a result, the viscosity prefactor (*A*) is given as 1.23 x 10^{-23} Pa^{-n} s^{-1} with *n* as 4. This produces a lower crust that has a lower viscosity in EXP-13 than EXP-1 (Fig S14A-B), which impacts the timing of fragment generation without actually fully rifting the upper crust (Fig S14C-D). However, the overall impact of the mechanism of generating continental fragments remains the same (Fig S14C-D) as strain from the mantle scar still manages to propagate through the weak lower crust.

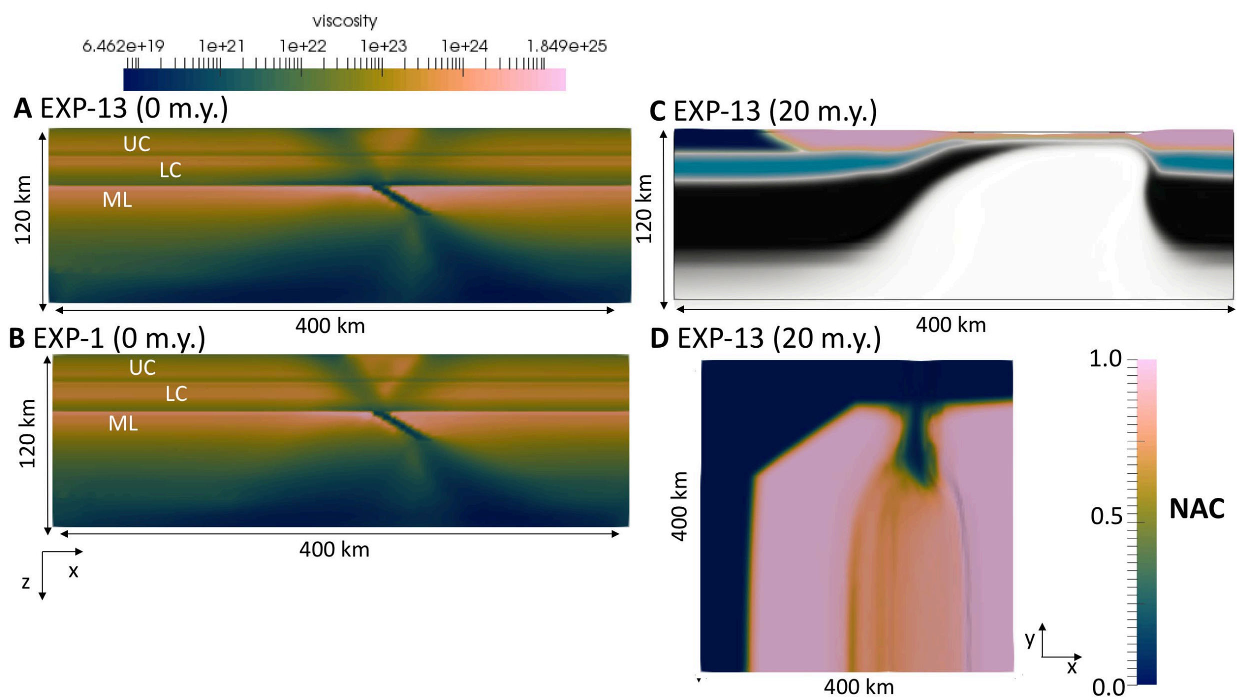

Figure S14: Impact of changing the rheology of the lower crust to that of Rybacki et al. (2006). A-B shows the initial viscosity profile of the lithosphere across the middle of the box for EXP-13 (A, Rybacki et al., 2006) and EXP-1 (B). EXP-13 has a lower viscosity lower mantle which takes into consideration the water fugacity of the material. C shows the composition deformation of the lithosphere after 20 m.y. for EXP-13. D shows the surface deformation of the North Atlantic Craton portion of the upper crust. Abbreviations: North Atlantic Craton; UC = upper crust; LC = lower crust; ML = mantle lithosphere.

Testing the model setup with 2D models

In a series of 2D models, we have tested a number of different factors that could potentially impact the mechanism for generating a continental fragment. In Figure S15 we explore the role of the depth of the mantle lithosphere scar, showing that the base of the scarring does not control the surface deformation (e.g., Fig S15A-D).

The mechanism for generating a continental fragment is based on the position of the mantle lithosphere scarring, as discussed above. Increasing the depth of the scar changes the tectonics of the rifting as the breakup is increased in the x-direction, as shown in EXP-15 (Fig S15E-F). In this model, a portion of the lower crust is exhumed to the surface as a result of the location of the strain deformation (Fig S15J).

Once the scar is deep enough to become part of the viscous mantle lithosphere, rather than within the strong, brittle portion of the mantle lithosphere), there is no deformation related to the mantle heterogeneity (Fig S15G-H). This is shown through the limited impact of the scar on the initial strain rate of the model (Fig S15H) as compared to models with weak structures in the brittle layer (Fig S15I-J).

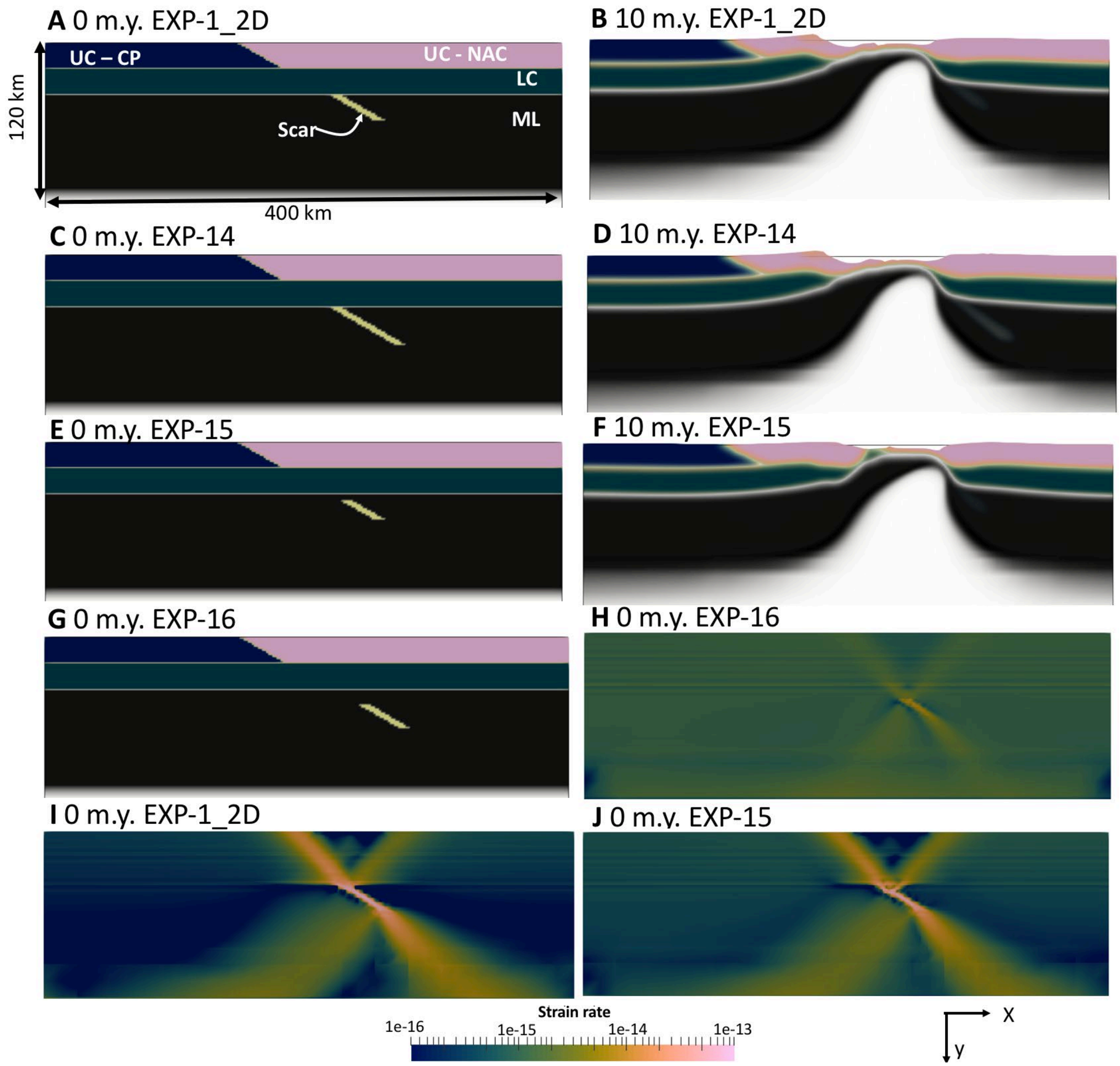

Figure S15: Impact of changing the position of the mantle lithosphere scar on tectonics in 2D models. Panels A, C, E and G show the initial condition for: the top 120 km of the 2D model for reference setup of a scar extending to a depth of 20 km from the lower crust boundary (A); model EXP-14 which has mantle lithosphere scar extending to a depth of 40 km from the lower crust boundary (C); model EXP-15 which has a shorter mantle lithosphere scar (10 km vertically) that starts 5 km deeper than the lower crust boundary (E); and EXP-16 which extends to a depth of 20 km vertically from 10 km deeper than the lower crust (G). Corresponding panels B, D, and F show the evolution of the lithosphere after 10 m.y. Panels H-J show the strain rate plots for the initial condition for models EXP-16 (H), EXP-1_2D (I) and EXP-15 (J).

Previous numerical studies have not established any consensus on the strain weakening parameters for continental rifting (e.g., Brune et al., 2014; Huismans & Beaumont, 2011; Naliboff & Buiter; Naliboff et al., 2020; Sandiford et al., 2021; Heron et al., 2019; Allken et al., 2013; Brune et al., 2013; Gouiza & Naliboff, 2021). To determine the impact of these parameters on the rifting process, seven previously published alternatives to EXP-1_2D were calculated (Table S5). Changes compared to the reference EXP-1_2D include: reducing the angle of internal friction (AIF) by 50% in EXP-17; reducing the cohesions by 50% in EXP-18; reducing both the cohesion and friction strain weakening factors (SAF) by 50% in EXP-19 (Brune et al., 2014; Huismans & Beaumont, 2011; Naliboff & Buiter; Naliboff et al., 2020; Sandiford et al., 2021); reducing the plasticity strain weakening intervals (PSWI) in EXP-20 (Heron et al., 2019); reducing both the AIF and PSWI in EXP-21 and 22 (Allken et al., 2013; Brune et al., 2013); increasing the cohesion SAF by 200% while reducing the friction SAF by 50% in EXP-23 (Gouiza & Naliboff, 2021).

Table S5: List of alternative 2D simulations to EXP-1_2D with changing strain weakening parameters in relation to Fig S16.

Model	Reference	Angle of Internal Friction	Cohesions	Plasticity strain weakening intervals	Cohesion strain weakening factors	Friction strain weakening factors
EXP-1_2D	Reference model; Pysklywec et al., 2002	30°	20 MPa	0.5 – 1.5	0.5	0.5
EXP-17		**15°**	20 MPa	0.5 – 1.5	0.5	0.5
EXP-18		30°	**10 MPa**	0.5 – 1.5	0.5	0.5
EXP-19	Brune et al., 2014; Huismans & Beaumont, 2011; Naliboff & Buiter; Naliboff et al., 2020; Sandiford et al., 2021	30°	20 MPa	0.5 – 1.5	**0.25**	**0.25**
EXP-20	Heron et al., 2019	30°	20 MPa	**0.0 – 0.5**	0.5	0.5
EXP-21	Allken et al., 2013	**15°**	20 MPa	**0.0 – 1.25**	0.5	0.5
EXP-22	Brune et al., 2013	**15°**	20 MPa	**0.05 – 1.0**	0.5	0.5
EXP-23	Gouiza & Naliboff, 2021	30°	20 MPa	0.5 – 1.5	**1.0**	**0.25**

Bold values show the parameters changed from the reference model (EXP-1).

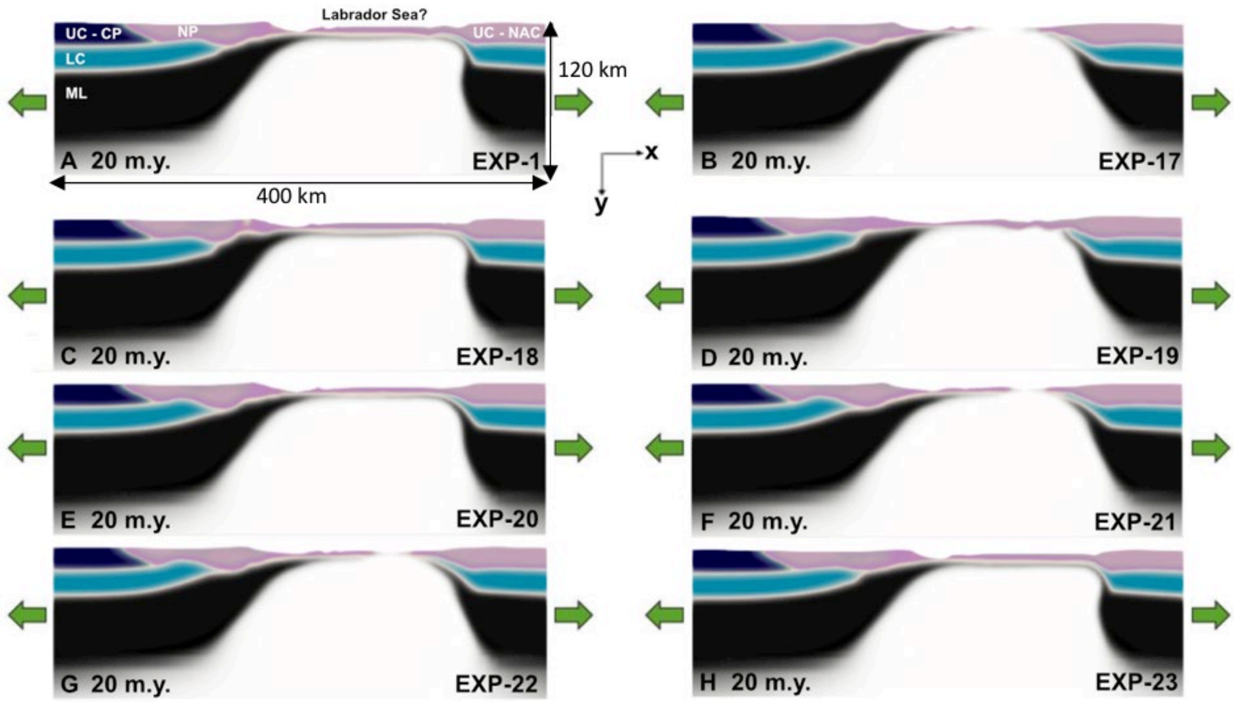

Figure S16: Impact of changing various strain weakening factors listed on Table S5 in a series of 2D models. Subfigures A-H show a timestamp of each lithospheric geometry at 20 m.y. after rift initiation. A: reference model EXP-1 in 2D; B: reduced angle of internal friction compared to EXP-1 (EXP-17); C: reduced cohesion as compared to EXP-1 (EXP-18); D: reduced strain weakening factors (EXP-19); E: reduced strain weakening intervals (0 – 0.5, EXP-20); F: reduced strain weakening intervals (0 – 1.25, EXP-21); G: reduced strain weakening intervals (0.05 – 1.0, EXP-22); H: increased cohesion weakening factor and reduced angle of internal friction strain weakening factor (EXP-23). Abbreviations: UC = upper crust; LC = lower crust; ML = mantle lithosphere; CP = SE Churchill Province. Uprising of materials from deeper mantle lithosphere and asthenosphere opens the model Labrador Sea.

There are some differences in the tectonic development between the models listed on Table S5 throughout their 25 m.y. evolution period, but tectonic structures remain comparable and does not impact the mechanism for generating a continental fragment (Figure S16). The development of the model Labrador Sea due to scar reactivation is present in all listed models, but the geometry of the underlying mantle lithosphere and asthenosphere uprising diverges between the models after the initial rift. A relatively symmetrical 'dome-shaped' uprising confined by the upper crusts appears at both 15° AIF (EXP-17, 21, and 22) and 50% cohesion and friction SWFs (EXP-19), while a modest east-offset in asymmetry is developed otherwise (Figure S16). A continental fragment generation of the model NAC is stranded to the CP during the thinning of the crust by extensional plate tectonic forces (Figure S16), and occurs in all models presented here. However, this fragment is completely detached to the model NAC at 20 m.y. at 15° AIF (EXP-17, 21, and 22) instead of retaining its attachment to the thinned NAC crust at 30° AIF (Figure S16) for these 2D models.

The deformation mechanisms within the mantle lithosphere and their impact on continental rifting have not been well resolved, and present some uncertainty surrounding our choice of rheology for this study. As a result, we constructed 2D models with a composite (harmonic average) of dislocation and diffusion creep of the viscous flow in the presence of a random initial strain perturbation (after Naliboff et al., 2020). The composite setup results in a more symmetrical rifting spreading from the lithospheric scar once the strain is localized (Figure S17B), which is different from the asymmetrical lithospheric deformation in the models with only dislocation creep (Figure 17A). Furthermore, rift development is much slower in the composite layers than the dislocation-only ones. However, unlike the dislocation-only model, the introduction of random initial strain perturbation accelerates the strain localization and the onset of rifting. Nonetheless, the above-mentioned NAC fragment is attached to the SE Churchill Province.

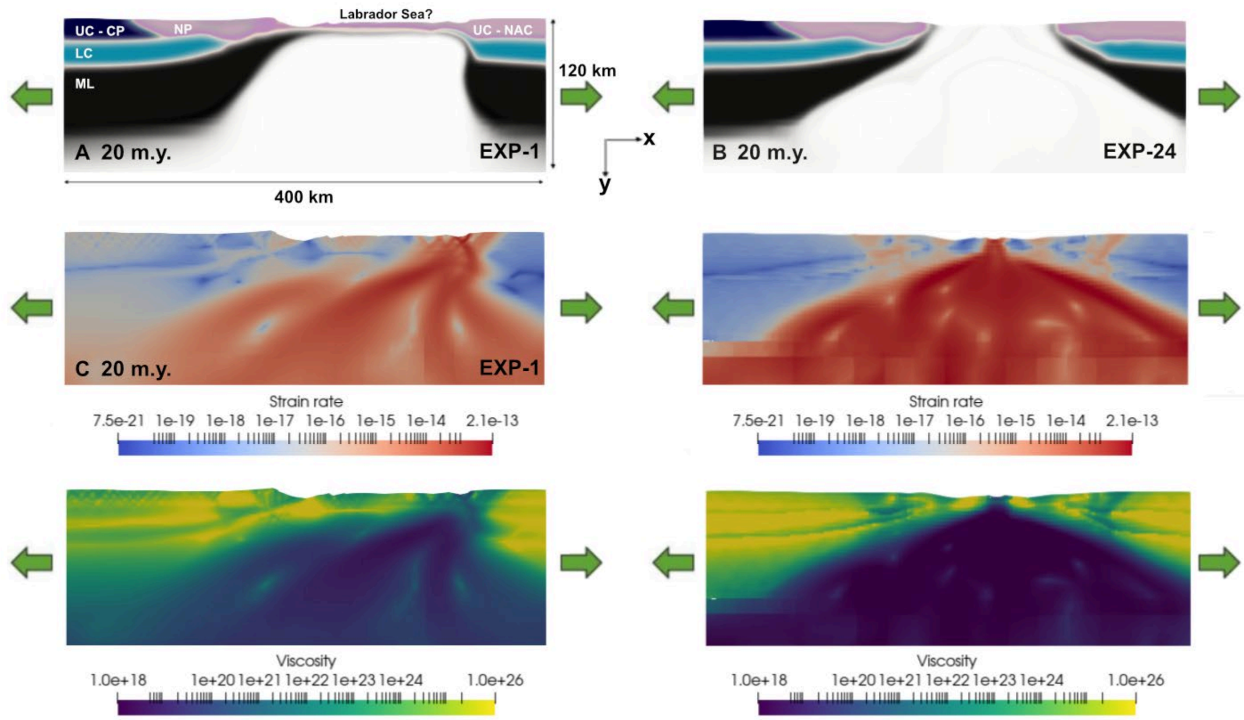

Figure S17: Impact of composite deformation mechanisms (dislocation and diffusion creep rheology) on tectonic development for 2D models. Subfigures A and B compare of the continental extension at 20 m.y. between the base EXP-1_2D and EXP-24 respectively. Subfigures C-D show strain rate and E -F show viscosity for the lithosphere. Abbreviations: UC = upper crust; LC = lower crust; ML = mantle lithosphere; CP = SE Churchill Province.

Figure S18 shows the impact of removing a composition in the upper crust (the model Churchill Province) to test whether any numerical instabilities could occur in the splitting up of the surface. Panels A and C show the initial condition for the top 120 km of the 2D model for reference setup EXP-1_2D and EXP-25 (which has only NAC at the surface), respectively. There is no difference between the two models, showing that the splitting of the surface into two compositions (which are the same) has no impact.

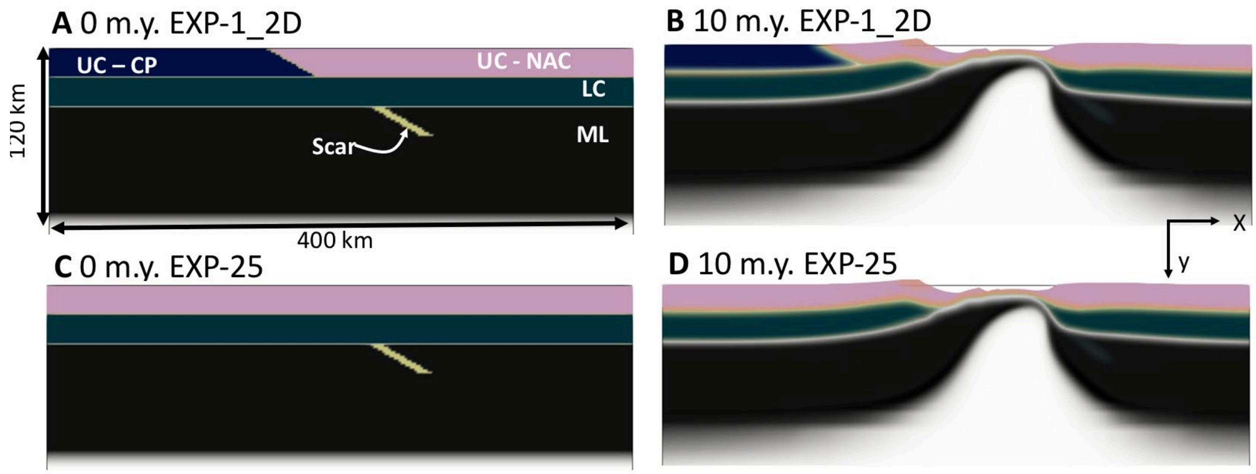

Figure S18: Impact of removing a composition in the upper crust (the model Churchill Province). Panels A and C show the initial condition for the top 120 km of the 2D model for reference setup EXP-1_2D and EXP-25 (which has only NAC at the surface), respectively. There is no difference between the two models, showing that the splitting of the surface into two compositions (which are the same) has no impact. Abbreviations: UC = upper crust; LC = lower crust; ML = mantle lithosphere; CP = SE Churchill Province.

In Figure S19, we explore the parameter for thermal expansivity. In the reference model EXP-1, thermal expansivity is set to 2×10^{-5} K^{-1} for all the compositions (following Naliboff et al. (2020) and Gouiza and Naliboff (2021)). However, there is some uncertainty in the appropriate values of thermal expansivity for the lithosphere - EXP-26 applies a value of 3×10^{-5} K^{-1} (Afonso et al., 2005) and EXP-27 applies an upper value of 3.5×10^{-5} K^{-1}. Changing the thermal expansivity in these models does not change the mechanism for generating a continental fragment (Figure S19).

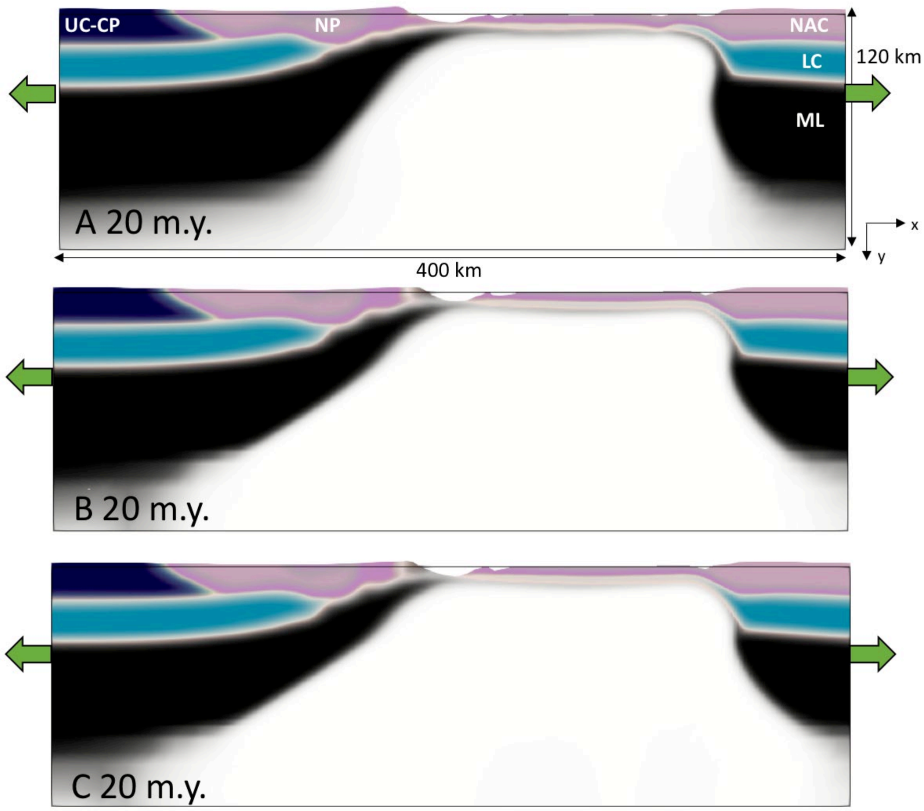

Figure S19: Impact of changing thermal expansivity, with one value used for all layers. Comparison of rifting of mantle suture from reactivation for different mantle lithosphere thermal expansivity (TE) values in 2D models. A: TE=2e-5 K^{-1} (EXP-1); B: TE=3e-5 K^{-1} (EXP-26); C: TE=3.5e-5 K^{-1} (EXP-27). Abbreviations: UC = upper crust; LC = lower crust; ML = mantle lithosphere; CP = SE Churchill Province; NP= Nain Province; NAC= North Atlantic Craton. Although the TE values vary for each model, there are no significant differences between each model.

Code, experimental inputs, and previous work comparison

This manuscript builds on the work from Heron et al. (2019) to better understand the process of generating the Nain Province - a continental fragment that originated from the opening of the Labrador Sea. After discussion on the rifting deformation of the Davis Strait it was clear that the same process could generate a continental fragment – here we have tested this theory as a potential blueprint for similar tectonic areas.

In modelling terms, there are some differences between the experiments of Heron et al. (2019) and this manuscript as the input parameters here have been updated or improved to be more in line with recent numerical modelling studies. The differences are outlined below:

- The angle of the mantle lithosphere scar is shallower (30º) in the current study as compared to Heron et al. (2019). This is an updated setup as the previous dip to the mantle lithosphere scar (45º) was on the upper end of the scar angles currently shown in the literature.
- In Heron et al. (2019), the crustal thickness was 30 km, whereas here we have updated the crustal size to be more in keeping with the lithospheric profile of the region (40 km, e.g., Gouiza and Naliboff, 2021).
- We updated the thermal profile of the initial condition to be based on the thermal profile of Naliboff et al., 2020 (changes to conductivity, layer temperatures, heat flux, and internal heating rate).
- We updated the rheological setup to be in line with Naliboff et al., 2020 (changes to thermal diffusivities and reference temperature).
- We updated the strain weakening parameters to be in line with Naliboff et al., 2020 (changes to cohesion, angle of internal friction, strain weakening intervals and factors).
- The spatial domain of the full model is smaller in the current study (400km x 400 km x 600 km rather than 800 km x 800 km x 600 km), as the Heron et al. (2019) box was too large to study the tectonic environments.
- We specify two separate upper crust compositions (NAC and Churchill Province). However, the parameters for both continental materials are the same.

Numerical code used

For these calculations we used ASPECT version 2.2.0, with dealii version 9.1.1. The version of ASPECT used can be found here
https://github.com/geodynamics/aspect

Another webpage for the ASPECT code can be found here:
https://aspect.geodynamics.org

The manual for the code has more detail about the inner workings and formulations, as well as information on benchmarking. The manual is available here:
http://www.math.clemson.edu/%7Eheister/manual.pdf -

Experimental inputs
The experiments were designed from the continental extension ASPECT cookbook:
https://github.com/geodynamics/aspect/blob/master/cookbooks/continental_extension.prm
And built on the paper by Naliboff et al., (2020):
https://github.com/naliboff/aspect/tree/naliboff_etal_2020_grl
The input files for this experiment can be found here:
https://github.com/heronphi/fragments2022

Animations

Animations of numerical model EXP1 can be found in the GitHub repository:
https://github.com/heronphi/fragments2022

- Surface_EXP1_EXP2 shows the surface evolution of NAC for model EXP1 and EXP2 in 1 Myr time outputs (e.g., Figure 3).
- Surface_Strain_EXP1_EXP2 shows the surface evolution of strain for model EXP1 and EXP2 in 1 Myr time outputs (e.g., Figure 3).
- Cross_EXP1 and Cross_EXP2 show the cross section across the middle of the box in 2 Myr time outputs, displaying composition evolution for models EXP1 and EXP2.
- Strain_cross_EXP1 shows the cross section across the middle of the box in 2 Myr time outputs, displaying strain rate and composition evolution.

References

Afonso, J. C., Ranalli, G., & Fernàndez, M. (2005). Thermal expansivity and elastic properties of the lithospheric mantle: results from mineral physics of composites. Physics of the Earth and Planetary Interiors, 149(3-4), 279–306. https://doi.org/https://doi.org/10.1016/j.pepi.2004.10.003

Allken, V., Huismans, R., & Thieulot, C. (2012). Factors controlling the mode of rift interaction in brittle-ductile coupled systems: A 3D numerical study. Geochemistry, Geophysics, Geosystems, 13(5). https://onlinelibrary.wiley.com/doi/full/10.1029/2012GC004077

Bangerth, W., Dannberg, J., Gassmoeller, R., & Heister, T. 2020. ASPECT v2.2.0. (version v2.2.0). Zenodo. https://doi.org/10.5281/ZENODO.3924604

Billen M.I., Hirth G. 2007. Rheologic controls on slab dynamics. Geochem. Geophys. Geosyst. 8:Q08012, doi: 10.1029/2007GC001597

Brune, S., Popov, A., & Sobolev, S. (2013). Quantifying the thermo-mechanical impact of plume arrival on continental break-up. Tectonophysics, 604, 51-59.

Brune, S., Heine, C., Pérez-Gussinyé, M., & Sobolev, S. (2014). Rift migration explains continental margin asymmetry and crustal hyper-extension. Nature Communications 2014 5:1, 5(1), 1-9. https://www.nature.com/articles/ncomms5014

Chapman, D., 1986. Thermal gradients in the continental crust. In: Dawson, J., Carswell, D., Hall, J., Wedepohl, K. (Eds.), The Nature of the Lower Continental Crust, vol. 24. Geol. Soc. Spec. Publ., pp. 63–70.

Christensen, U.R., 1992. An Eulerian technique of thermomechanical modeling of lithospheric extension, J. geophys. Rex, 97, 2015-2036.

Cook, F. A., R. M. Clowes, D. B. Snyder, A. J. van der Velden, K. W. Hall, P. Erdmer, and C. Evenchick (2004), Precambrian crust and lithosphere beneath the Northern Canadian Cordillera discovered by LITHOPROBE seismic reflection profiling, Tectonics, 23, TC2010, doi:10.1029/2002TC001412.

Donea, J. and Huerta, A., 2003, Finite element methods for flow problems, John Wiley & Sons, Ltd, doi:10.1002/0470013826.

Funck, T., Louden, K. E. & Reid, I. D., 2001. Crustal structure of the Grenville Province in southeastern Labrador from refraction seismic data: evidence for a high-velocity lower crustal wedge. Can. J. Earth Sci. 38, 1463–1478.

Gleason, G. C., & Tullis, J. (1995). A flow law for dislocation creep of quartz aggregates determined with the molten salt cell. Tectonophysics, 472, 213–225.

Glerum, A., Thieulot, C., Fraters, M., Blom, C., and Spakman, W., 2017, Implementing nonlinear viscoplasticity in ASPECT: benchmarking and applications to 3D subduction modeling, Solid Earth Discuss., https://doi.org/10.5194/se-2017-9.

Gouiza, M., and Naliboff, J., 2021, Rheological inheritance controls the formation of segmented rifted margins in cratonic lithosphere: Nature communications, v. 12, p. 1–9.

Heister, T., Dannberg, J., Gassmoller, R., Bangerth, W., 2017, High accuracy mantle convection simulation through modern numerical methods – II: realistic models and problems. Geophys. J. Int. 210, 833–851.

Heron, P.J., Pysklywec, R.N., and Stephenson, R., 2016a, Lasting mantle scars lead to perennial plate tectonics: Nature Communications, v. 7, p. 11834, https://doi.org/10.1038/ncomms11834 .

Heron, P. J., R. N. Pysklywec, and R. Stephenson, 2016b, Identifying mantle lithosphere inheritance in controlling intraplate orogenesis, J. Geophys. Res. (Solid Earth), 6966–6987, doi:10.1002/2016JB013460.
Hirth, G. and Kohlstedt, D., 2003, Rheology of the upper mantle and the mantle wedge: a view from the experimentalists. In: Eiler, J. (Ed.), Inside the Subduction Fac- tory. In: Geophys. Monogr. Am. Geophys. Soc., vol. 138, pp. 83–105.
Huismans, R., & Beaumont, C. (2011). Depth-dependent extension, two-stage breakup and cratonic underplating at rifted margins. Nature 2011 473:7345, 473(7345), 74-78. https://www.nature.com/articles/nature09988
Kachanov, L. M., 2004, Fundamentals of the Theory of Plasticity, Dover Publications, Inc..
Kronbichler, M., Heister, T., and Bangerth, W., 2012, High accuracy mantle convection simulation through modern numerical methods, Geophysical Journal International, 191, 12–29.
Naliboff, J., and S. J. H. Buiter, 2015, Rift reactivation and migration during multiphase extension, Earth Planet. Sci. Lett., 421, 58–67, doi:10.1016/j.epsl.2015.03.050.
Naliboff, J. B., Glerum, A., Brune, S., Péron-Pinvidic, G., & Wrona, T. (2020). Development of 3-D rift heterogeneity through fault network evolution. Geophysical Research Letters, 47, e2019GL086611. https://doi.org/ 10.1029/2019GL086611
Pysklywec, R.N., Beaumont, C., Fullsack, P., 2002. Lithospheric deformation during the early stages of continental collision: Numerical experiments and comparison with South Island, New Zealand. J. Geophys. Res. Solid Earth 107, ETG 3-1-ETG 3-19. https://doi.org/10.1029/2001JB000252
Pysklywec, R., Beaumont, C., 2004, Intraplate tectonics: feedback between radioactive thermal weakening and crustal deformation driven by mantle lithosphere instabilities. Earth Planet. Sci. Lett. 221, 275–292.
Rose, I., Buffett, B., & Heister, T. (2017). Stability and accuracy of free surface time integration in viscous flows. Physics of the Earth and Planetary Interiors, 262, 90–100. doi:10.1016/j.pepi.2016.11.007
Rybacki, E., Gottschalk, M., Wirth, R., Dresen, G., 2006, Influence of water fugacity and activation volume on the flow properties of fine-grained anorthite aggregates. J. Geophys. Res. 111 (B3).
Sandiford, D., Brune, S., Glerum, A., Naliboff, J., & Whittaker, J. (2021). Kinematics of Footwall Exhumation at Oceanic Detachment faults: Solid-Block Rotation and Apparent Unbending. Geochemistry, Geophysics, Geosystems, 22(4), e2021GC009681. https://onlinelibrary.wiley.com/doi/full/10.1029/2021GC009681.
Scott, D. J. 1998, An overview of the UPb geochronology of the Paleoproterozoic Torngat Orogen, Northeastern Canada. Precambrian Research 91.1-2, 91-107.
Thieulot, C., 2011, FANTOM: Two- and three-dimensional numerical modelling of creeping flows for the solution of geological problems, Physics of the Earth and Planetary Interiors, 188, 47–68.
Thomas, W.A., 2010, Interactions between the southern Appalachian–Ouachita orogenic belt and basement faults in the orogenic footwall and foreland, in Tollo, R.P., Bartholomew, M.J., Hibbard, J.P., and Karabinos, P.M., eds., From Rodinia to Pangea: The lithotectonic record of the Appalachian region: Geological Society of America Memoir 206, p. 897–916, doi:10.1130/2010.1206(34).

Welford, J. K. & Hall, J., 2013. Lithospheric structure of the Labrador Sea from constrained 3-D gravity inversion. Geophys. J. Int. 195, 767–784.

Willett, S. D., 1992, Dynamic and kinematic growth and change of a Coulomb wedge, in: Thrust tectonics, edited by McClay, K. R., pp. 19–32, Chapman and Hall, New York.